33RD CONGRESS
OF THE INTERNATIONAL COUNCIL
OF THE AERONAUTICAL SCIENCES
STOCKHOLM, SWEDEN, 4-9 SEPTEMBER, 2022

STRAKE SECTION IMPACT ON HYBRID-DELTA-WING AERODYNAMICS

Dominik Sedlacek & Christian Breitamter

Chair of Aerodynamics and Fluid Mechanics, Technical University of Munich, 85748 Garching, Germany

Abstract

High agility aircraft often exhibit a highly swept leading edge extension in front of a medium swept main wing to allow for high maneuverability. In this study, the effect of the strake length on the vortex formation, interaction and breakdown is investigated regarding two double-delta wing and two triple-delta wing configurations. To analyze the influence of the strake length, force and moment measurements and particle image velocimetry experiments are conducted. It is shown that the short strake length leads to a more upstream and less abrupt vortex breakdown for both configuration types. A significant stabilizing effect is observed for the strake vortex at the double-delta wing configuration at low to medium angles of attack. This is caused by the vortex-vortex interaction. The long-strake variants exhibit lateral stability at higher angles of attack. But for the double-delta wing with long strake, the rolling moment reversal occurs very abrupt and hardly controllable. This behavior is alleviated by the shortening of the strake.

Keywords: Hybrid Delta Wing, Vortex interaction, Strake influence

1. Introduction

The rising scope of performance and maneuverability requirements for high agility aircraft leads to enhanced design challenges. Typically, these configurations feature low aspect-ratio with small to sharp leading edge radii, medium to high leading-edge sweeps and a delta wing planform [1]. This kind of planform allows for the exploitation of nonlinear lift increase and for maneuverability at high angles of attack. This is caused by the separation and formation of leading-edge vortices. The vortices induce high axial velocities in the vortex core and high suction peaks at the wing surface. At medium to high angles of attack depending on the leading-edge sweep, the vortices start to burst above the wing. This results in a loss of suction starting at the rear part of the wing but with further increase in angle of attack, the breakdown location moves upstream [2]. The breakdown characteristics can change between vortices separating at nonslender or semislender wings, $50^\circ < \varphi < 60^\circ$ and vortices separating at slender wings, $\varphi > 60^\circ$ [3, 4]. Vortices developing at leading edges with a high sweep angle are more stable at higher angles of attack but exhibit an abrupt vortex breakdown which can cause critical flight mechanical instabilities. Vortices separating at nonslender or semislender leading edges are characterized by a more gradual vortex breakdown at lower angles of attack [5].To combine the positive effects of both vortex types, modern high agility aircraft often feature a highly swept leading-edge extension or strake in front of a medium swept main wing. Consequently, a vortex separates at the slender strake section and another one separates at the main wing. The interaction of those vortices results in a stabilization of both vortices and a shift of breakdown to higher angles of attack [6]. The abruptness of the vortex breakdown can be reduced depending on the planform parameters like leading-edge sweep, strake length, et cetera. Therefore, it is important to comprehend the effect of the vortex-vortex interaction on the stability of the vortices and the characteristics of the vortex breakdown.

Brennenstuhl and Hummel [7] investigated the effect of different double-delta wing configurations. The analysis focused on the flow field developing at wing planforms with strake and at the effect of the strake length. It was shown that the merging of the vortices occurs at higher angles of attack for longer strakes, that both vortices have a stabilizing effect and that wings with constant span have similar breakdown characteristics despite different leading-edge sweeps. Further investigations on the flow field at different double-delta wing configurations were conducted in Refs. [8, 9, 10].

A further approach for improving maneuverability is to introduce a short medium swept wing section in front of the strake. This leads to a vortex formation at a medium swept leading-edge and at the transition to the highly swept strake, the vortex follows the kink. The result is a stabilization of the vortex but a less abrupt vortex breakdown compared to a double-delta wing configuration [6]. These kind of configurations are investigated in Refs. [11, 12, 13]. In this study, particle image velocimetry (PIV) and force and moment measurements were conducted to analyze the influence of the strake length on vortex formation, interaction, and breakdown at a double- and a triple-delta wing configuration at a Reynolds number of $Re = 3.0 \cdot 10^6$ and a Mach number of $Ma = 0.15$. These experiments were conducted at symmetric freestream conditions at an angle of sideslip of $\beta = 0^\circ$ and at asymmetric freestream conditions, $\beta = 5^\circ$ at several angles of attack. The flow field, the flow topology and the flight mechanical stability characteristics for the long-strake configurations are extensively discussed in Refs. [6] and [14].

2. Configuration

In this study, four generic wing-fuselage configurations are considered. The examined configurations, Figure 1, are two double-delta-wing configurations the so-called W2 configurations and two triple-delta-wing configurations, W1. The model wing consists of flat plates with a sharp leading-edge. The W2 configuration, Figure 1a, is characterized by a high leading-edge sweep $\varphi_2 = 75^\circ$ in the front part (strake), and a rear wing section with a medium leading-edge sweep $\varphi_3 = 52.5^\circ$. The length of the strake section differs between both configurations, $l_2/c_r = 0.475$ for the long strake configuration, W2_STLong, and $l_2/c_r = 0.375$ for the short one, W2_STShort. The W1, Figure 1b, consists of three wing segments of different leading-edge sweep: The front part with a medium leading-edge sweep of $\varphi_1 = 52.5^\circ$, followed by a strake with a high leading-edge sweep of $\varphi_2 = 75^\circ$ and the rear wing section with similar wing sweep as the front section, $\varphi_1 = \varphi_3$. The two configurations differ in the length of strake l_2, the long strake configuration, W1_STLong, with $l_2/c_r = 0.35$ and the short one, W1_STShort, with $l_2/c_r = 0.25$. The modular setup of the wind-tunnel model allows for the deployment of leading-edge flaps (slats) at different angles at the main wing, shown in Figure 1. For this study a deflection angle of $\eta_3 = 22.5^\circ$ is chosen. The most important geometrical parameters of the configurations are summarized in Table 1 [6].

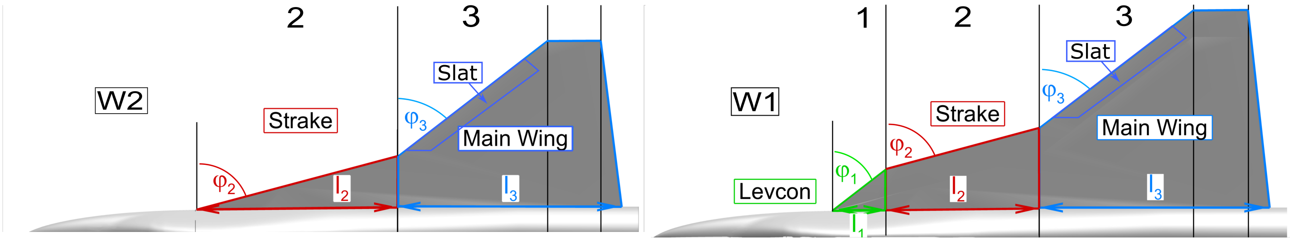

(a) W2

(b) W1

Figure 1 – Double- and triple-delta wing planforms.

Table 1 – Geometrical parameters of the W2 and W1 configurations.

		W2		W1	
		STShort	STLong	STShort	STLong
c_r	$[m]$	0.802	0.802	0.802	0.802
s	$[m]$	0.345	0.367	0.395	0.417
S_{Ref}	$[m^2]$	0.279	0.266	0.344	0.329
l_t	$[m]$	1.350	1.350	1.350	1.350
Λ	$[-]$	0.175	0.160	0.160	0.145
l_μ	$[m]$	0.471	0.426	0.512	0.468
l_1/c_r	$[-]$	-	-	0.125	0.125
l_2/c_r	$[-]$	0.375	0.475	0.250	0.350
l_3'/c_r	$[-]$	0.350	0.350	0.350	0.350
l_3/c_r	$[-]$	0.625	0.525	0.625	0.525
φ_1	$[^\circ]$	-	-	52	52
φ_2	$[^\circ]$	75	75	75	75
φ_3	$[^\circ]$	52	52	52	52
$x_{ref,Bal}/c_r$	$[-]$	0.540	0.540	0.540	0.540
x_{CG}/c_r	$[-]$	0.569	0.599	0.551	0.579

3. Experimental Technique

The experimental methods have already been published in [14]. The experiments were conducted in the wind tunnel A (WT-A) of the Technical University of Munich. The WT-A features an open test section with a cross section of $1.80\,m \times 2.40\,m$ and a length of $4.80\,m$. The wind tunnel reaches a maximum velocity of $U_{WT-A} = 65\,m/s$ and provides a turbulence level below 0.4%. To set the angle of attack α, the angle of sideslip β and the roll angle γ, a three-component model support is used. The angle of sideslip and roll angle can be adjusted within $\pm 90^\circ$. The possible range for the angle of attack is limited to $\alpha = 0^\circ - 40^\circ$. The maximum blockage at $\alpha = 40^\circ$ is $4.9\,\%$ of the wind-tunnel cross section.

For the measurements, a freestream velocity of $U_\infty = 48\,m/s$, a Mach number of $Ma = 0.15$ and a Reynolds number of $Re = 3.0 \cdot 10^6$ based on the reference length $l_{Re} = 1\,m$ was used. The following will be a short overview of the used configurations, the six-component balance, the PIV setup, and the approach on oil flow visualization.

3.1 Force and Moment Measurements

An internal six-component strain-gauge balance was used to acquire the aerodynamic forces and moments. The maximum sustainable loads read $900\,N$, $450\,N$, $2500\,N$ for axial, lateral, and normal forces, respectively. The maximum sustainable moments are $120\,Nm$, $160\,Nm$, $120\,Nm$ for rolling, pitching, and yawing moments, respectively. The forces and moments were measured with a sampling frequency $f_m = 800\,Hz$ for a total acquisition time of $t_m = 10\,s$. The accuracy of the aerodynamic coefficients for the applied test setup is presented in Table 2 with respect to repeatability. The repeatability is defined as the standard deviation of the coefficients determined from several angle of attack polar measurements. The standard deviation was determined for every angle of attack and

Table 2 – Repeatability of measured force and moment coefficients.

ΔC_D	ΔC_Y	ΔC_L	ΔC_{mx}	ΔC_{my}	ΔC_{mz}
± 0.0035	± 0.0012	± 0.0051	± 0.0005	± 0.0017	± 0.00042

coefficient. The force and moment measurements presented in the following refer to the mean values of the acquired series of measurements per angle of attack.[14]

3.2 Stereo Particle Image Velocimetry

The flow field above the wing is measured in several crossflow sections by a stereo particle image velocimetry (PIV) measurement system. All three velocity components are obtained. For the adjustment of the measured plane, the Stereo-PIV system was mounted on a three axis traversing system next to the wind tunnel test section, see Figure 2a. For an alignment of the cameras and the laser sheet with the angle of attack of the wind tunnel model, the cameras and laser sheet can be rotated around the Y-axis of the traversing system. The two sCMOS cameras have a resolution of 2560×2160 pixel and were placed up- and downstream of the measurement plane with an angle of 60°. The sCMOS sensor planes were tilted by Scheimpflug adapters to meet the Scheimpflug criterion, cf. [15]. Seeding particles with a diameter of $\approx 1\ \mu m$ were infused into the flow. The cameras recorded 400 image pairs per cross section with a sampling frequency of $f_m = 15\ Hz$. The presented results are the mean values determined by the 400 samples. The uncertainties of the mean velocity components were quantified to $|u_{err}/U_\infty| < 0.06$ and $|v_{err}/U_\infty| = |w_{err}/U_\infty| < 0.035$ [16]. Figure 2b shows the position of the measured crossflow sections for both configurations. [14]

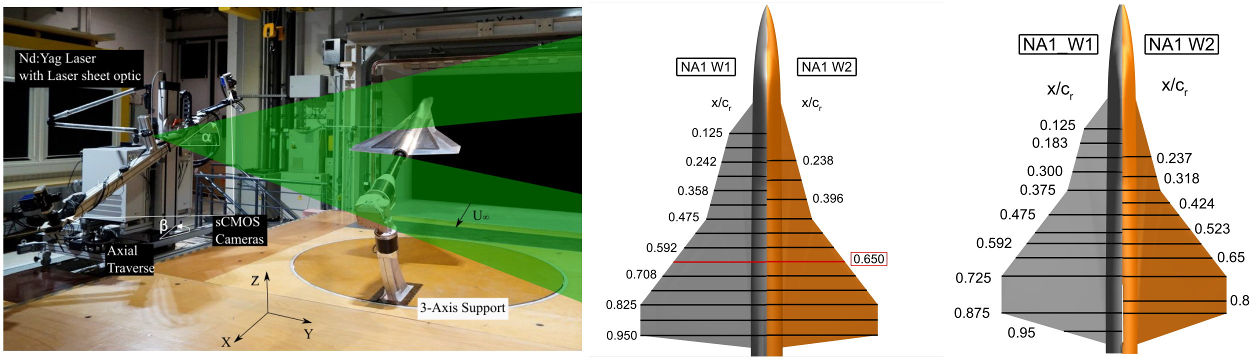

(a) (b) STLong [6] (c) STShort

Figure 2 – a) Stereo-PIV measurement setup [6] and b) as well as c) measured crossflow sections for long and short strake configurations, respectively.

4. Double Delta Wing - W2

In this chapter, the flow field, vortex breakdown locations, the longitudinal as well as the lateral stability characteristics and the slat effects at the described double-delta wing configurations will be analyzed. As previously mentioned, the long-strake configuration is already discussed in [6] and [14]. Therefore, the discussion will focus on the short-strake configuration and the influence of the strake length.

4.1 Flow Field Analysis at Symmetric Freestream Conditions

The flow fields for different angles of attack $\alpha = \{8^\circ, 16^\circ, 24^\circ, 32^\circ\}$ are presented in Figure 3 for W2_STShort and in Figure 4 for W2_STLong. The flow field is illustrated by means of the nondimensional axial vorticity and areas of stagnating flow with a nondimensional axial velocity of $0 < u/U_\infty < 0.2$ are displayed in pink as well as in black for reversed flow, $u/U_\infty < 0$. Both configurations exhibit a comparable flow field. At the strake section, the flow separates and the so-called inboard vortex (IBV) forms. At $x/c_r = 0.475$, the leading-edge sweep changes from $\varphi = 75^\circ$ to $\varphi = 52.5^\circ$. At this point, the IBV is disconnected from the leading-edge shear layer and a second primary vortex develops, the so-called midboard vortex (MBV). At $\alpha = 8^\circ$, the movement of both vortices is in straight direction with no indication of vortex-vortex interaction. Compared to the long-strake variant, the IBV vanishes at $x/c_r \approx 0.725$. This indicates a vortex breakdown already at $\alpha = 8^\circ$. The IBV core vorticity is decreasing rapidly and the IBV becomes unstable above the wing without energy entrainment by the leading-edge shear layer. For the long-strake variant, both vortices are stable above the entire wing. At $\alpha = 16^\circ$, both, short- and long-strake, configurations induce strong vortex-vortex interactions.

The vortices rotate around each other, and both are stable above the entire wing. The IBV of the W2_STShort is stabilized by the vortex-vortex interaction and no breakdown occurs. Both configurations exhibit a similar flow field but for the W2_STShort configuration, the rotation of the vortices is faster. The MBV has reached its most inboard location at $x/c_r \approx 0.65$, $\Delta x/c_r \approx 0.275$ after the kink for the short-strake configuration and at $x/c_r \approx 0.825$, $\Delta x/c_r \approx 0.35$ after the kink for the long-strake variant. Furthermore, at W2_STShort, the approaching maxima of the axial vorticity indicate the merging of IBV and MBV in the rear part of the wing.

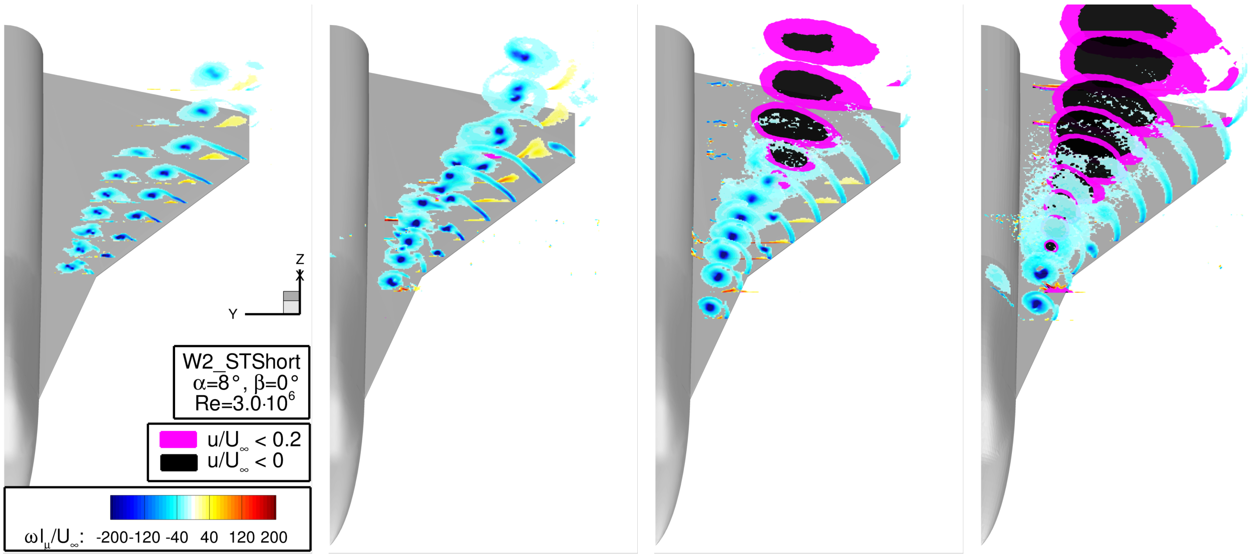

(a) $\alpha = 8^\circ$ (b) $\alpha = 16^\circ$ (c) $\alpha = 24^\circ$ (d) $\alpha = 32^\circ$

Figure 3 – Non-dimensional axial vorticity $\omega\, l_\mu/U_\infty$ and axial velocity u/U_∞ distributions of the W2_STShort configuration at different α and $\beta = 0^\circ$.

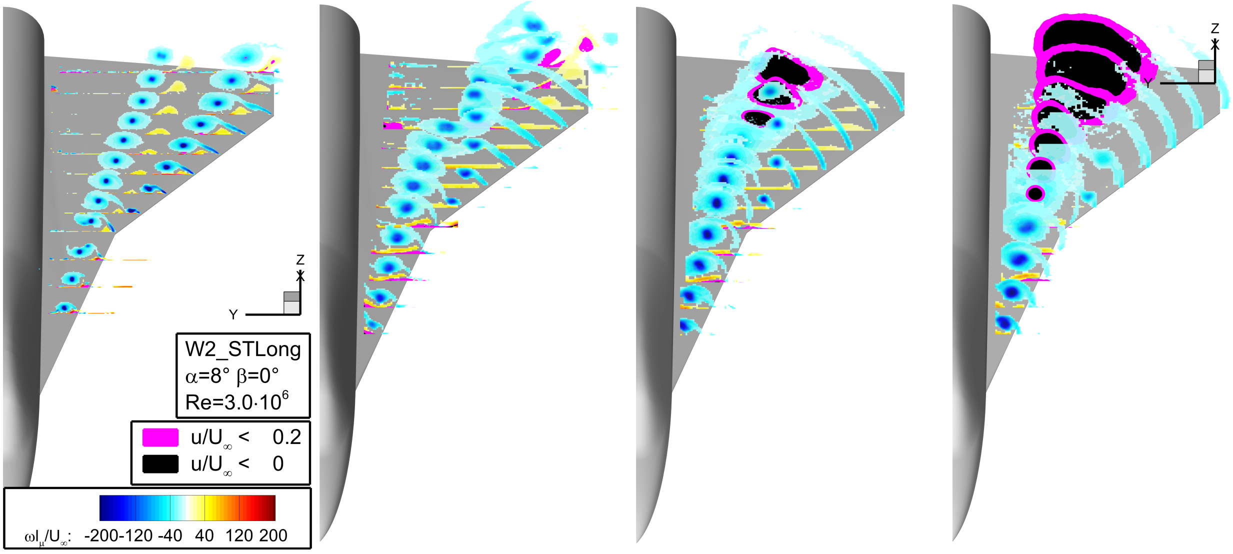

(a) $\alpha = 8^\circ$ (b) $\alpha = 16^\circ$ (c) $\alpha = 24^\circ$ (d) $\alpha = 32^\circ$

Figure 4 – Non-dimensional axial vorticity $\omega\, l_\mu/U_\infty$ and axial velocity u/U_∞ distributions of the W2_STLong configuration at different α and $\beta = 0^\circ$.

With an increase in angle of attack to $\alpha = 24^\circ$, vortex breakdown occurs for both, short- and long-strake, configurations indicated by the black area illustrating reverse flow. The IBV at the short-strake configuration bursts more upstream compared to W2_STLong. This results in a larger area of reversed flow. In both cases, the MBV bursts directly downstream of the IBV.

At $\alpha = 32°$, the flow field is dominated by the wake of the burst vortices. For both configurations, the vortex breakdown occurs at the transition to the lower swept leading-edge and a large wake area forms downstream.

4.2 Flow Field Analysis at Asymmetric Freestream Conditions

In this section, the flow field at the double-delta wing configurations at an angle of sideslip of $\beta = 5°$ is discussed. Figure 5 shows the vortex-dominated flow field by means of the nondimensional axial vorticity and areas of stagnating or reverse flow in pink and black, respectively. The W2_STShort configuration is illustrated in Figures 5a to 5c. At $\alpha = 16°$, the flow field at the leeward side is comparable to the symmetric freestream case. A strong interaction is observable between the vortices, and both stay stable above the entire wing. The merging of the vortices is shifted more upstream and the maxima in axial vorticity merge completely in the rear part of the wing. At the windward side, the vortex system breaks down abruptly at $x/c_r \approx 0.733$ due to the reduced effective sweep angle. The long-strake configuration shows a similar flow field with a more downstream located vortex breakdown at the windward side.

With an increase to $\alpha = 24°$, the vortex breakdown at the windward side and the vortex merging at the leeward side is shifted more upstream. At the long-strake configuration, the vortices merge at the leeward side for the first time.

At $\alpha = 32°$, the windward side is dominated by separated and reverse flow for both, short and long-strake variants and no vortices are developing. However, on the leeward side the vortex system is developing fully stable over the entire wing at W2_STLong with bursting of the vortex system at $x/c_r \approx 0.6$.

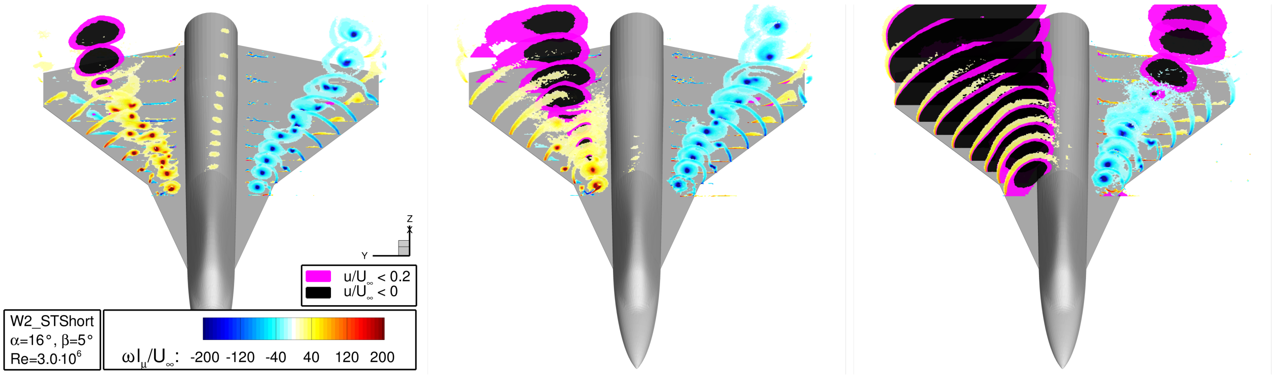

(a) W2_STShort $\alpha = 16°$ (b) W2_STShort $\alpha = 24°$ (c) W2_STShort $\alpha = 32°$

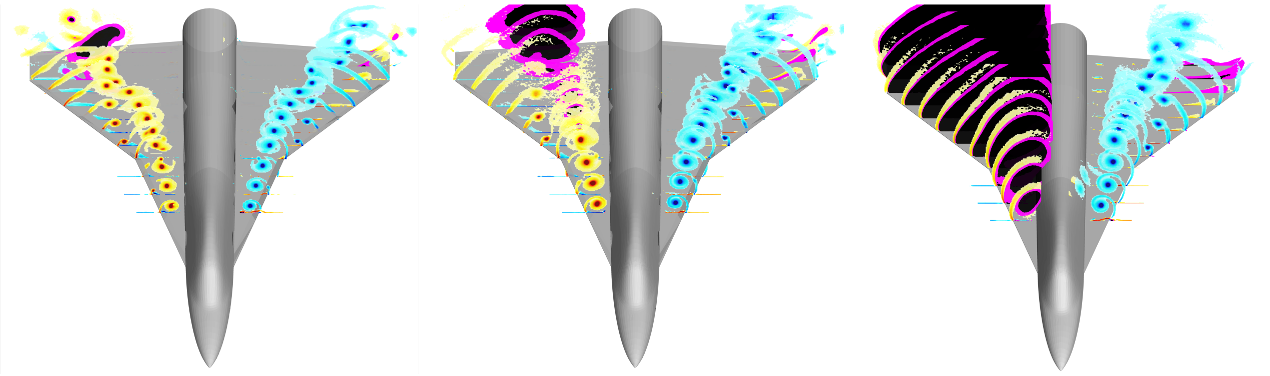

(d) W2_STLong $\alpha = 16°$ (e) W2_STLong $\alpha = 24°$ (f) W2_STLong $\alpha = 32°$

Figure 5 – Non-dimensional axial vorticity $\omega\, l_\mu / U_\infty$ and axial velocity u/U_∞ distributions of the double-delta wing configurations at different α and $\beta = 5°$.

4.3 Vortex Breakdown Characteristics

In this section, the vortex breakdown locations are discussed at symmetric and asymmetric freestream conditions for the double-delta wing configurations. Figure 6 shows the vortex breakdown locations as function of the angle of attack in solid lines for W2_STLong and in dash-dot lines for the short-strake variant. The different breakdown locations at different angles of sideslip are shown and are compared to single-delta wing configurations published by Kohlman and Wentz [5]. The definition of vortex breakdown varies between vortices forming at slender or nonslender leading edges. At slender wings, the vortex breakdown occurs more abrupt, and the location is defined by the first appearance of negative axial velocities in the vortex core. The breakdown of vortices separating from nonslender leading edges is determined by the change from jet- to wake-type vortex core flow. Therefore, reverse vortex core flow is not necessary [4]. The breakdown locations of the IBV are shown in Figure 6a. At $\alpha = 8^\circ$, vortex breakdown related to the short-strake variant occurs at significantly lower angles of attack compared to single-delta wings and the long-strake configuration due to the separation from the shear layer entrainment and the shorter strake length. After the kink between strake and main wing, the IBV of both configurations is weakening and the axial vorticity is alleviating but at W2_STLong the vortex is still stable at the trailing edge. The longer strake allows for the development of a stronger vortex and therefore, the long-strake IBV is able to stay stable over a longer distance separated from shear layer entrainment. With increasing angle of attack, the vortices start to interact and the IBV is entrained with energy from the MBV interaction. This leads to a more stable IBV and vortex merging. The breakdown locations for $\beta = -5^\circ$ represent the IBV breakdown locations at the windward side shown in Figure 5. At $\alpha = 16^\circ$, the vortex breakdown occurs more upstream at W2_STShort. And both configurations can be compared to the vortex breakdown locations of a 60°-swept single delta wing. With further increase in angle of attack, the vortex breakdown moves more upstream and occurs first at both configurations for the symmetric freestream conditions. The shift between the breakdown location at $\beta = -5^\circ$ is decreasing due to the abrupt and quick upstream shift of vortex breakdown for vortices developing at slender wings. At $\alpha = 32^\circ$, vortex breakdown of both, short- and long-strake, configurations at symmetric freestream conditions occurs at the kink between strake and main wing which is comparable to the breakdown locations at the windward side at $\alpha = 24^\circ$. As discussed in subsection 4.2, no vortex formation occurs at $\beta = -5^\circ$ which indicates the vortex breakdown reaching the apex. At the leeward side, $\beta = -5^\circ$, no vortex breakdown occurs except for the W2_STShort configuration at $\alpha = 32^\circ$.

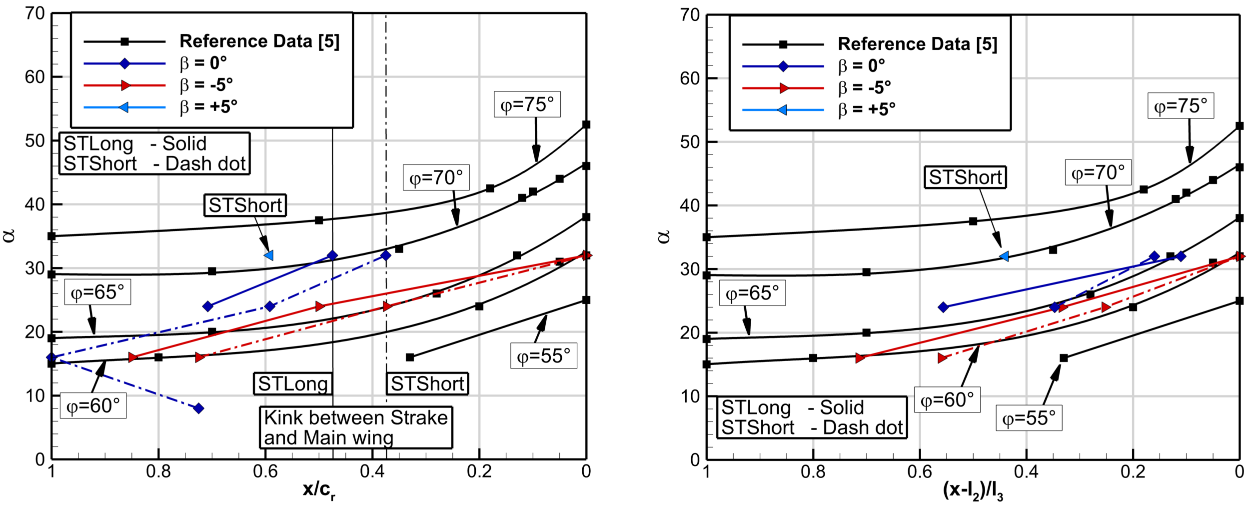

(a) Location of the IBV breakdown

(b) Location of the MBV breakdown

Figure 6 – Vortex-breakdown locations relative to root chord for varying angle of attack for the W2 configurations at $Re = 3.0 \cdot 10^6$. Including reference data taken from [5], [6] and [14].

The breakdown locations of the MBV are presented in Figure 6b starting at the leading-edge kink for a better comparison to the single-delta wings. The locations show a similar behavior. The $\beta = -5^\circ$ cases exhibit a more upstream vortex breakdown and fit with the data of a 60°-swept single delta wing. The breakdown locations of the MBV are locked to the breakdown positions of the IBV due to the influence of abrupt vortex breakdown and merging of the vortex systems leading to a common vortex system breakdown. However, it is clearly observable that the MBV exhibit a vortex breakdown at significantly higher angles of attack compared to single-delta wings with similar leading-edge sweep. The stabilizing effect of the vortex interactions leads to an effective sweep increase of $\Delta\varphi_{eff} \approx 12°$. Due to the different configurations and pure delta wings without fuselage, the results are not directly comparable but give an indication on the planform effects on vortex breakdown for comparable configurations. However, the interactions result in a significant increase in vortex stability and the decrease in strake length reduces this effect.

4.4 Longitudinal and Lateral Stability Characteristics

In this section, the longitudinal and lateral stability characteristics are discussed by means of force and moment coefficients and their derivatives for symmetric and asymmetric freestream conditions. First, an analysis of the moment reference point for the pitching moment is conducted. Figure 7 shows the pitching moment for different reference point locations. In previous publications, cf. [6] and [14], the reference point of the balance, $x_{ref,bal}$, is commonly used. This point is positioned at $x/c_r = 0.54$ or at $71\ \%$ of the total configuration length. It is also the basis for the shift of the reference point illustrated as solid line in case of movement in positive x-direction and dash-dot line for the negative x-direction. The red line represents the pitching moment coefficient with the surface centroid of the configuration as reference point. The latter is located at $x/c_r = 0.569$, $+2\ \%\ l_t$ of the balance reference point, for W2_STShort and at $x/c_r = 0.599$, $+3.5\ \%\ l_t$ of $x_{ref,bal}$, for the long-strake configuration. The default pitching moment of W2_STShort exhibits a positive pitching moment coefficient over the whole range of angles of attack and the long-strake variant a mostly negative pitching moment coefficient. This is caused by the different percentage of lift-generating surfaces upstream of the moment reference point. Regarding the W2_STLong configuration, only $20\ \%$ of the wing surface are positioned upstream of the reference point. For the short-strake variant, on the other hand, $30\ \%$ of the surface are upstream of the reference point. Therefore, the centroid is needed for a surface-independent consideration. For the short-strake configuration, most polars exhibit a positive pitching moment coefficient and an upstream shift of the reference point of at least $\approx 2\ \%$ is needed for a negative pitching moment. The polar with a reference point located $-2.5\ \%\ l_t$ upstream of the balance reference point is close to the center of pressure. The W2_STLong configuration exhibits a negative pitching moment coefficient for $\alpha < 24°$ and a reference point shift of $\Delta x_{ref} < +1\ \%\ l_t$, see Figure 7b. Compared to the W2_STLong, the short-strake configuration exhibits a more linear distribution of the pitching moment and the up- and downstream shift lead to a smaller range of pitching moment variation. The short-strake configuration exhibits a maximum difference of $\Delta C_{my,xref} = 0.384$, and the long-strake variant of $\Delta C_{my,xref} = 0.456$. This indicates a higher stability in case of a shift of the reference point regarding W2_STShort. Due to the strong vortex interaction and the abrupt vortex breakdown, the pitching moment of the long-strake configuration exhibits a more volatile behavior.

The longitudinal characteristics at symmetric freestream conditions are shown in Figure 8. Figure 8a shows the lift coefficient C_L, black, and the pitching moment coefficient, blue, for the long-, filled square icons, and the short-strake configurations, white triangles. The lift and pitching moment derivatives are presented in Figure 8b, the axis of pitching moment derivative is reversed for better visual illustration. For $\alpha < 10°$, both configurations show a similar behavior regarding the lift coefficient polar with a slightly higher lift for the long-strake variant. For this range, the pitching moment coefficient shows an almost linear behavior for W2_STShort. For $\alpha > 8°$, the W2_STLong configuration exhibits a decrease in pitching moment caused by the strong vortex interaction in the rear part of the wing. With further increase in angle of attack, the long-strake configuration generates more lift especially beyond the vortex breakdown for the short-strake configuration at $\alpha \approx 18°$, see Figure 8b. Vortex breakdown does not affect the pitching moment derivative as significantly as for the long-strake variant. At $\alpha = 24°$, the lift coefficient of the long-strake configuration decreases abruptly indicating an abrupt vortex breakdown. In this region, the pitching moment derivative also has a peak, and the pitching moment coefficient exceeds the short-strake variant. The maximum angle of attack is reached at $\alpha_{max} = 32°$ for both configurations with a maximum lift coefficient of $C_{L,max} = 1.31$ and $C_{L,max} = 1.41$ for the short- and long-strake configuration, respectively.

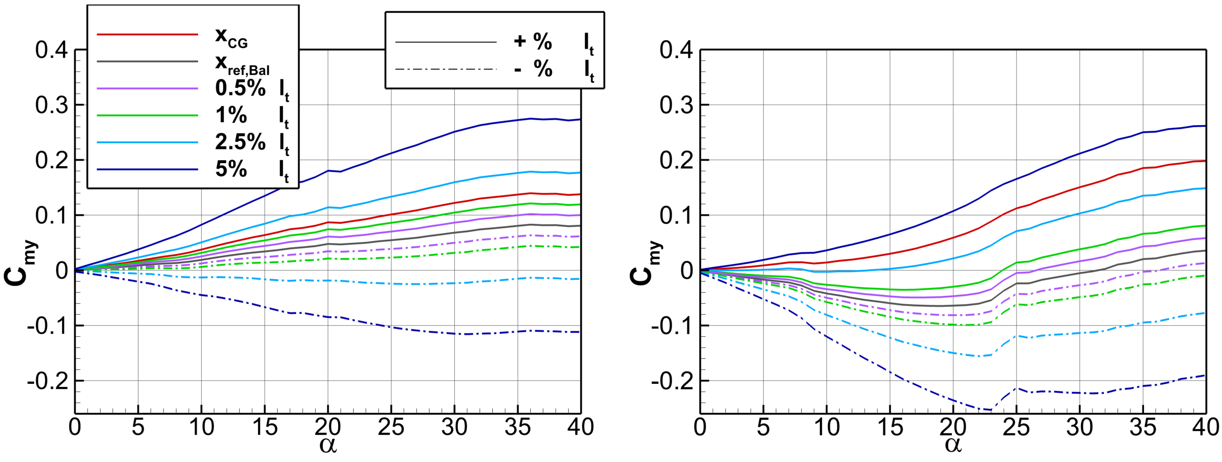

(a) STShort (b) STLong

Figure 7 – Variation of the reference point of the pitching moment.

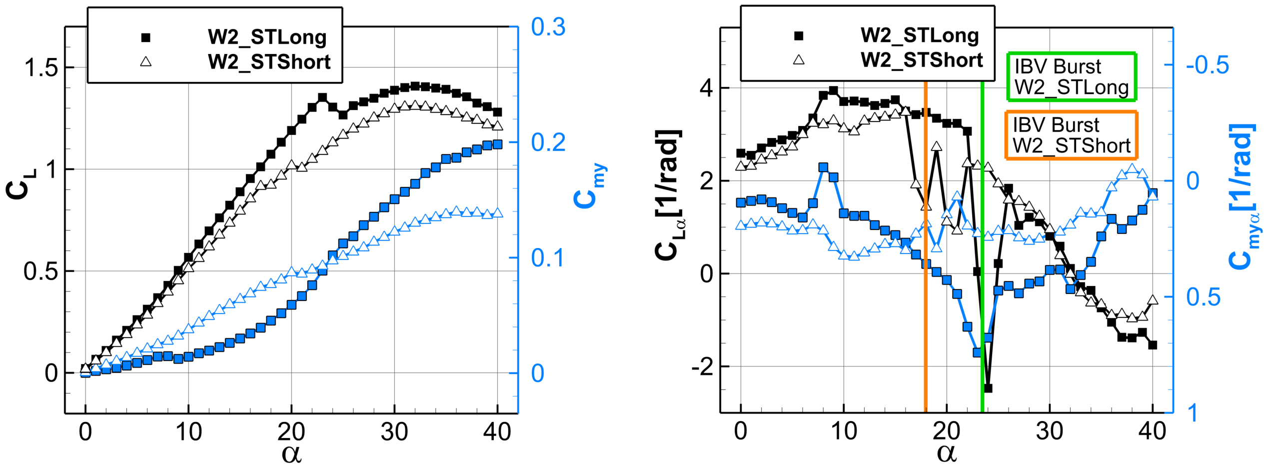

(a) Lift coefficient C_L (b) Lift- $C_{L\alpha}$ and Pitching Moment derivative $C_{my\alpha}$

Figure 8 – Longitudinal aerodynamic coefficients and derivatives for the W2_STShort and W2_STLong configurations versus α at $\beta = 0°$.

The longitudinal force and moment coefficients at an angle of sideslip of $\beta = 5°$ are shown in Figure 9a. The lift coefficient shows a behavior comparable to the symmetric case. The abrupt lift decrease caused by vortex breakdown at the windward side occurs at lower angles of attack and is smoother. At very high angles of attack, both configurations exhibit a further increase in lift coefficient due to the stable vortex systems at the leeward side. The breakdown of the vortex system leads to immediate lift reduction. The maximum angle of attack is reached at $\alpha_{max} = 33°$ and $\alpha_{max} = 36°$ with a maximum lift coefficient of $C_{L,max} = 1.37$ and $C_{L,max} = 1.45$ for the short- and long-strake configuration, respectively. The pitching moment coefficient shows a similar behavior for both configurations with a lower pitching moment coefficient for the long-strake configuration at lower angles of attack and an earlier and less abrupt vortex breakdown at the W2_STShort configuration.

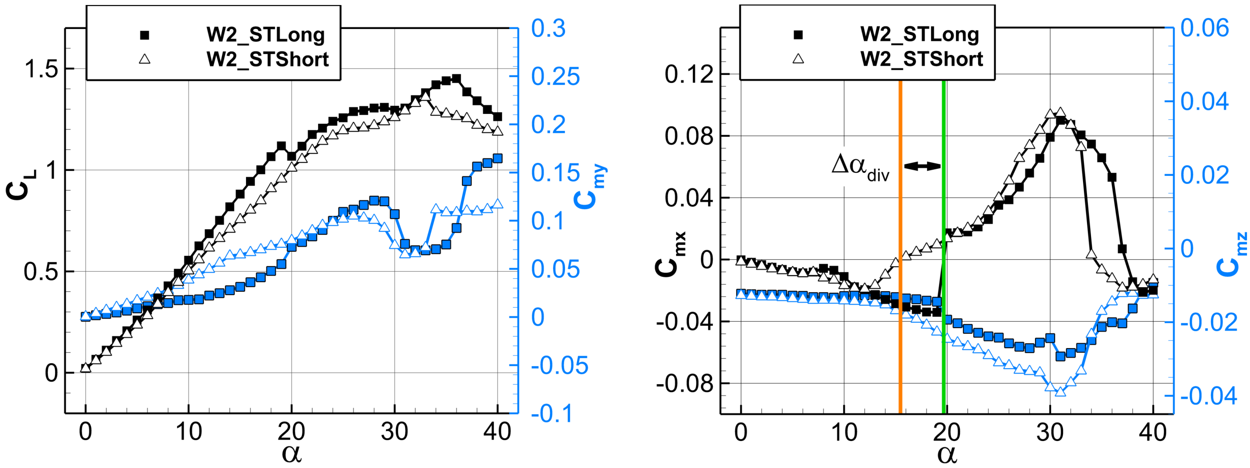

(a) Longitudinal coefficients for lift C_L and pitching moment coefficient C_{my}

(b) Lateral coefficients for rolling C_{mz} and yawing moment C_{mz}

Figure 9 – Longitudinal and lateral aerodynamic coefficients for the W2_STShort and W2_STLong configurations versus α at $\beta = 5^\circ$.

The rolling moment, black line and icons, and the yawing moment coefficient, blue line and icons, are shown in Figure 9b. The rolling moment exhibits negative values at low angles of attack. This indicates a right wing up movement. With vortex breakdown at the windward side, at $\alpha \approx 14^\circ$ and $\alpha \approx 19^\circ$ for the short- and long-strake configuration, respectively, the rolling moment increases. At the transition to a positive rolling moment, the so-called rolling moment reversal, lateral stability cannot not be guaranteed. This change is marked by the angle of divergence, illustrated as orange line at $\alpha \approx 16^\circ$ and green line at $\alpha \approx 20^\circ$ for the short- and long-strake configuration, respectively. This indicates a lateral stability at higher angles of attack for W2_STLong but with an abrupt and hardly controllable rolling moment reversal. At higher angles of attack, the yawing and rolling moment characteristics are comparable.

4.5 Influence on Slat Efficiency

The influence of the deployed slats at an deflection angle of $\eta_3 = 22.5^\circ$ on the force and moment characteristics is shown in Figure 10. Figure 10a presents the differences in lift coefficient between the slat configuration (SL22) and the default configuration (SL00). The results are shown for both short- and long-strake configurations at symmetric and asymmetric freestream conditions, $\beta = 0^\circ, 5^\circ$. In the range of $\alpha < 8^\circ$, all configuration polars show a similar behavior. The slat configuration generates less lift than the default configurations and for $\alpha > 6^\circ$ the difference increases. The effect of the delayed vortex formation at the main wing and especially the vortex interaction leads to a lift decrease for SL22 of $\Delta C_L \approx -0.18$ for the long-strake variant at $\alpha = 22^\circ$ and of $\Delta C_L \approx -0.16$ for W2_STShort. For the long-strake default configuration at $\beta = 0^\circ$, the abrupt vortex breakdown results in a significant lift decrease. In combination with a further lift increase at the SL22 configuration, the difference in lift coefficient between SL22 and SL00 configuration becomes positive and, therefore, more lift is generated at the SL22 configuration. The lift increase due to deployed slats is highest at $\alpha \approx 28^\circ$. This indicates a vortex breakdown at $\alpha \approx 28^\circ$ at $\beta = 0^\circ$ for the W2_STLong with deployed slats and, therefore, an increase in the angle of attack related to vortex breakdown of $\Delta\alpha_B \approx 5^\circ$ and an increase in maximum lift coefficient of $C_{L,max} \approx 0.07$. At angles of attack of $\alpha > 28^\circ$, the lift coefficient for the SL22 configurations decreases significantly and the efficiency of the slats is reduced.

Compared to the W2_STLong configuration, the short-strake variant exhibits a lower maximum lift increase due to slat deployment, $\Delta C_L \approx 0.08$. Due to the less abrupt vortex breakdown, the change between highest negative difference and highest positive difference is more gradual, $\Delta\alpha \approx 9^\circ$ compared to the long-strake configuration, $\Delta\alpha \approx 6^\circ$. At very high angles of attack, $\alpha > 32^\circ$, both configurations exhibit a quite constant lift increase, $\Delta C_L \approx 0.5 - 0.6$ due to deployed slats.

Considering the angle of sideslip, the lift gain for the SL22 compared to SL00 exhibits two discrete peaks at both configurations. For the long-strake variant the peaks are at $\alpha \approx 29^\circ$, $\Delta C_L \approx 0.12$, and at $\alpha \approx 38^\circ$, $\Delta C_L \approx 0.16$. In this case, the first peak represents the vortex breakdown at the windward side at higher angles of attack and the second one the delayed vortex breakdown at the leeward side. Between the peaks, the lift increase gained by the slats vanishes mostly. For the short-strake configuration, the peaks occur at lower angles of attack $\alpha_1 \approx 28^\circ$ and $\alpha_2 \approx 35^\circ$ and are lower $\Delta C_{L,1} \approx 0.09$ and $\Delta C_{L,2} \approx 0.15$. These results indicate a higher efficiency of the slats at the long-strake variant. However, this configuration exhibits an abrupt increase in lift in the range of $23^\circ < \alpha < 25^\circ$.

In Figure 10b, the rolling moment coefficient is presented to the long- and short-strake double-delta wing configuration with and without deployed slats. The deployment of the slats leads to a significant increase in the angle of divergence especially for the short-strake variant. The angle of the rolling moment reversal α_{div} is increased by $\Delta\alpha_{div,Slat} \approx 9^\circ$ for the W2_STShort and $\Delta\alpha_{div,Slat} \approx 5^\circ$ for the long-strake variant. Furthermore, the abruptness of the rolling moment reversal, regarding especially the W2_STLong, is reduced. This leads to a more controllable flight behavior at asymmetric freestream conditions due to the deployment of slats.

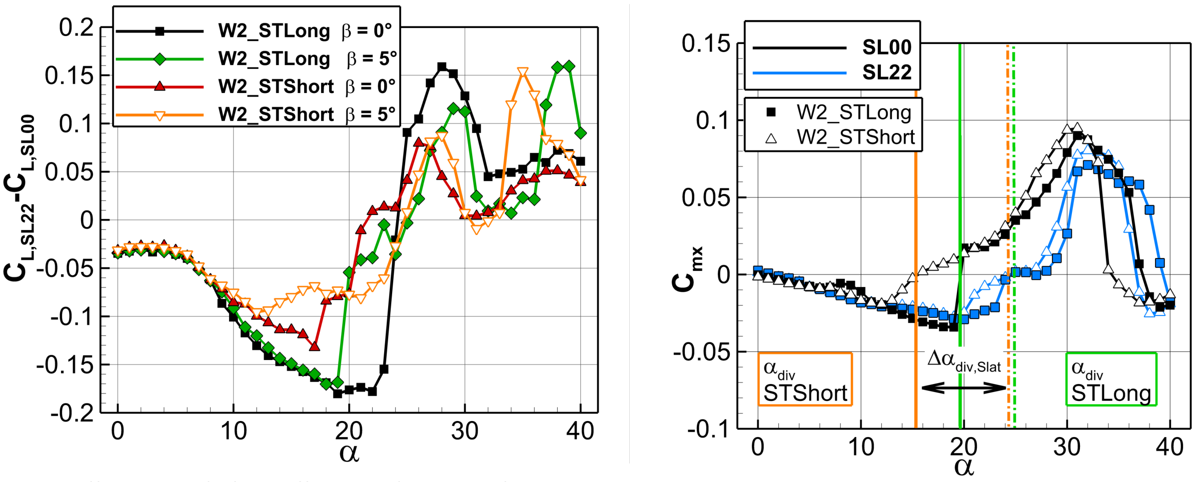

(a) Difference of lift coefficient of slat configuration (SL22) and default configuration as function of the angle of attack

(b) Lateral coefficients for rolling C_{mz} and angle of divergence

Figure 10 – Slat efficiency and influence on longitudinal and lateral aerodynamic coefficients for the W2_STShort and W2_STLong configurations versus α.

5. Triple Delta Wing - W1

In this chapter, the flow field, vortex breakdown locations, the longitudinal as well as the lateral stability characteristics and slat effects at the described triple-delta wing configurations will be analyzed. As previously mentioned, the long strake configuration has already been discussed in [6] and [14]. Therefore, the discussion will focus on the short-strake configuration and the influence of the strake length.

5.1 Flow Field Analysis at Symmetric Freestream Conditions

The flow field at the triple-delta wing configurations at $\beta = 0^\circ$ is to some extent comparable to the double-delta wing configurations. The IBV separates at the lower swept front-wing section and the MBV at the main wing. At an angle of $\alpha = 8^\circ$, both vortices exhibit an almost linear vortex axis above the wing. The IBV bursts at both, short- and long-strake, configurations. The MBV is stable above the entire wing for W1_STLong and bursts at $x/c_r \approx 0.725$ for the W1_STShort configuration. At $\alpha = 16^\circ$, the vortices interact with each other and the MBV moves inboard above the IBV. The vortex breakdown occurs more upstream for the short-strake variant. The more upstream located vortex breakdown results in a decrease in vortex interaction. Reverse flow occurs only downstream of the breakdown of the MBV, and the fusion of both breakdown regions leads to large areas with reverse flow.

At $\alpha = 24^\circ$, vortex breakdown moves more upstream and the wake-type IBV core flow exhibits negative axial velocities at $x/c_r \approx 0.3$ for the short-strake configuration. With the breakdown of the MBV, the wake increases significantly. At the long-strake variant, the vortex breakdown occurs more downstream. This implies a strong upstream influence of the strake length on the IBV above the front part of the strake. The MBV breakdown occurs more downstream at W1_STLong indicating a still higher stabilization effect despite the IBV breakdown.

With a further increase in angle of attack by $\alpha = 8^\circ$, see Figure 11d and Figure 12d, the vortex cross section increases and with a more upstream vortex breakdown, the area of reverse flow in the vortex core increases. The development of the MBV at W1_STShort is hardly observable due to the early breakdown. The MBV at W1_STLong is slightly more stable. In both cases, the flow field is dominated by a wake-type IBV with reverse core flow and the wake of the burst vortices.

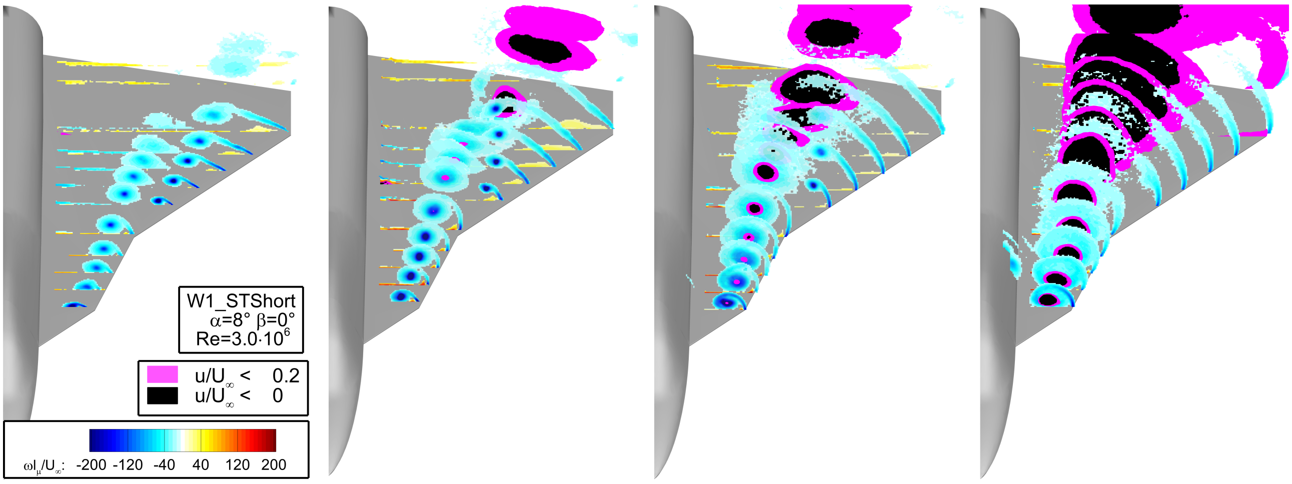

(a) $\alpha = 8^\circ$ (b) $\alpha = 16^\circ$ (c) $\alpha = 24^\circ$ (d) $\alpha = 32^\circ$

Figure 11 – Non-dimensional axial vorticity $\omega\, l_\mu / U_\infty$ and axial velocity u/U_∞ distributions of the W1_STShort configuration at different α and $\beta = 0^\circ$.

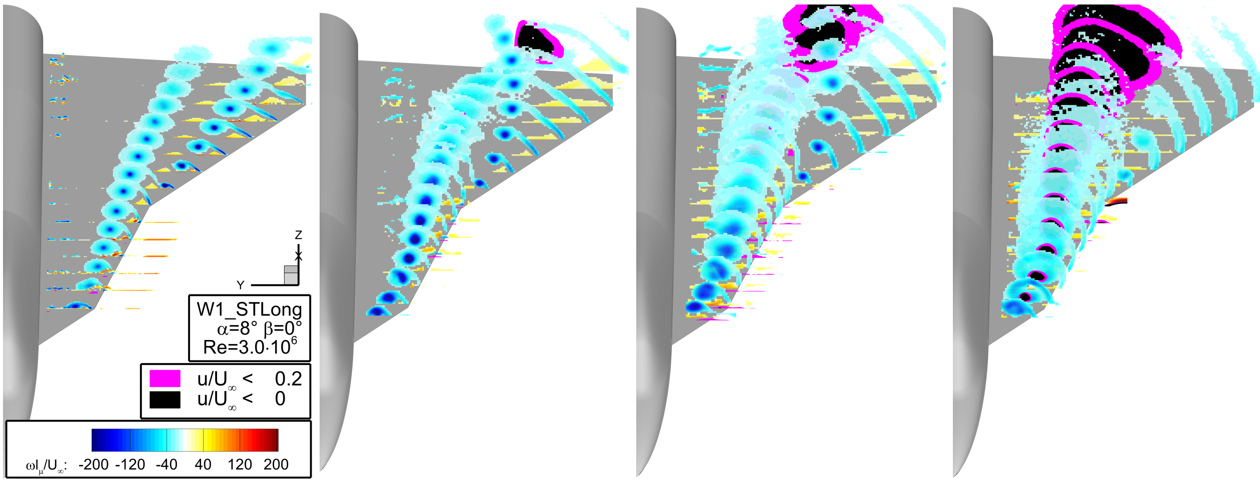

(a) $\alpha = 8^\circ$ (b) $\alpha = 16^\circ$ (c) $\alpha = 24^\circ$ (d) $\alpha = 32^\circ$

Figure 12 – Non-dimensional axial vorticity $\omega\, l_\mu / U_\infty$ and axial velocity u/U_∞ distributions of the W1_STLong configuration at different α and $\beta = 0^\circ$.

5.2 Flow Field Analysis at Asymmetric Freestream Conditions

To analyze the influence of asymmetric freestream conditions, the flow field at an angle of sideslip of $\beta = 5^\circ$ is investigated. Figure 13 shows the non-dimensional axial vorticity and the nondimensional axial velocity distributions at several cross sections for both configurations at $\alpha = \{16^\circ, 24^\circ, 32^\circ\}$. The flow field at the windward side at $\alpha = 16^\circ$ is comparable to the symmetric case. The IBV bursts at the main wing kink at $x/c_r \approx 0.375$ for the short-strake configuration and more upstream for W1_STLong.

For the latter, the MBV breakdown occurs close to the trailing edge and the fusion of the vortex wake does not lead to reverse flow. For the W1_STShort configuration, the breakdown of the MBV combined with the IBV wake leads to a large area of reverse flow but located more downstream compared to the symmetric case. Therefore, the breakdown of the vortices developing at a lower effective leading-edge sweep are more gradual and the decrease of effective sweep leads to a more upstream breakdown at the long-strake configuration which counteracts the previous findings. At the leeward side, the vortex systems are stable for both configurations. This indicates that the increase in effective leading-edge sweep on the leeward side leads to a vortex system which is stable for a significantly longer distance whereas the decrease in effective sweep at the windward side results in a minor upstream shift of the breakdown positions.

At $\alpha = 24^\circ$, see Figure 13b and Figure 13e, the vortex breakdown at the windward side is shifted more upstream. At both configurations, the core flow is reversed in the first examined cross section. However, the MBV at W1_STLong is more stable, and the breakdown occurs more downstream. At the leeward side of the long-strake configuration, the IBV breakdown is observable at $x/c_r \approx 0.66$ and the MBV is stable above the wing. At the short-strake variant, the IBV breaks down more upstream than at the windward side at $\alpha = 16^\circ$ and the reversal of the core flow occurs also more upstream. However, the vortex wakes do not merge, and the area of reversed flow is significantly smaller compared to the windward side at $\alpha = 16^\circ$.

Comparable to the double-delta wing configuration, at the windward side at $\alpha = 32^\circ$, cf. Figure 13c and Figure 13f, the flow is completely separated, and no vortex development occurs. At the leeward side, the fuselage vortex is observable for both, short- and long-strake configurations and is moving below the IBV in outside direction. The fuselage vortex at the long-strake configuration is interacting with the developing MBV directly downstream of the first leading-edge kink at $x/c_r = 0.475$. At W1_STShort, the fuselage vortex is interacting with the shear layer and the MBV more downstream of the kink. The MBV shows a more stable behavior compared to the MBV at the long-strake variant indicating a MBV destabilization by the fuselage vortex.

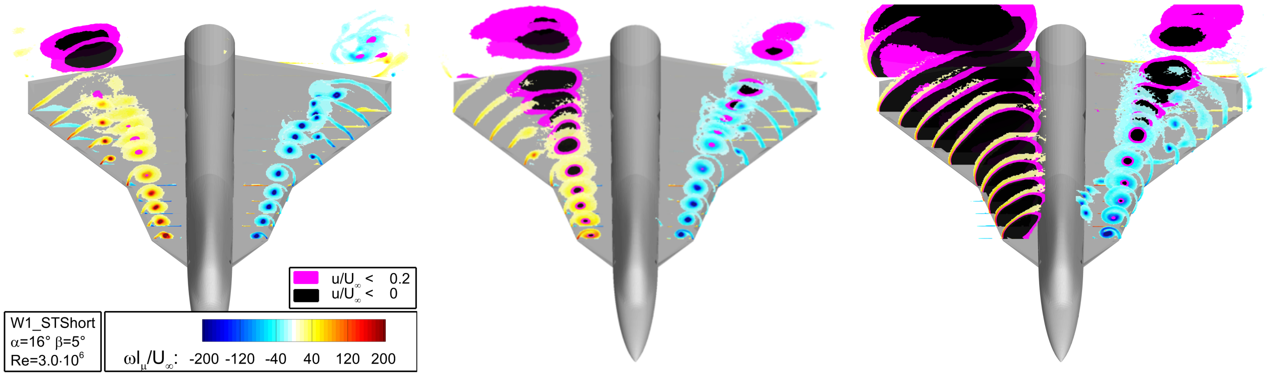

(a) W1_STShort $\alpha = 16^\circ$ (b) W1_STShort $\alpha = 24^\circ$ (c) W1_STShort $\alpha = 32^\circ$

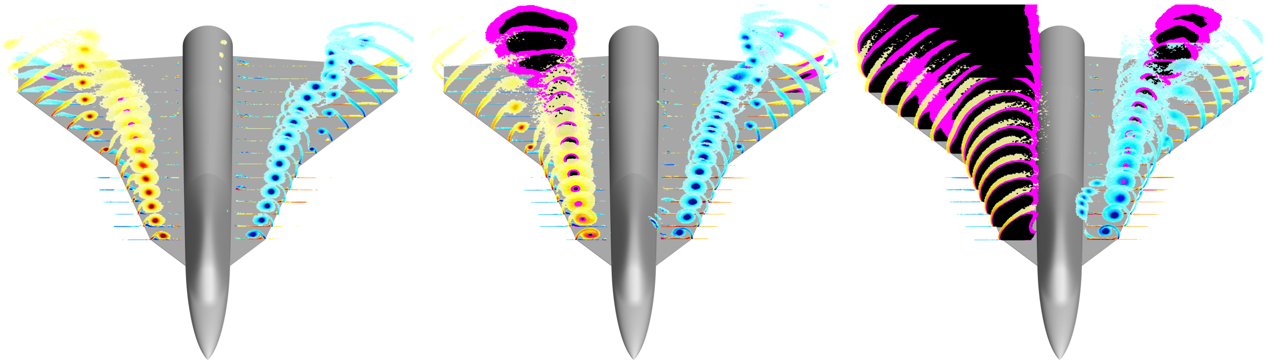

(d) W1_STLong $\alpha = 16^\circ$ (e) W1_STLong $\alpha = 24^\circ$ (f) W1_STLong $\alpha = 32^\circ$

Figure 13 – Non-dimensional axial vorticity $\omega\, l_\mu / U_\infty$ and axial velocity u/U_∞ distributions of the W1_STLong configuration at different α and $\beta = 5^\circ$.

5.3 Vortex Breakdown Characteristics

The vortex breakdown locations of both, short- and long-strake, configurations are shown in Figure 14 at symmetric, $\beta = 0^\circ$, and asymmetric freestream conditions, $\beta = -5^\circ$ and $\beta = +5^\circ$ for the windward and the leeward side, respectively. The W1_STLong is illustrated by a solid line and the W1_STShort by a dash-dot line. The IBV at both configurations bursts at $\alpha = 8^\circ$. With an increase in angle of attack, both locations move more upstream but the IBV at the long-strake configuration burst now directly downstream of the IBV at the short-strake configuration. With further increase in angle of attack the IBV at W1_STLong is shifted slower upstream and, therefore, the breakdown locations diverge again. The change in angle of sideslip to $\beta = +5^\circ$ leads to a stabilization especially at lower and medium angles of attack. At $\alpha > 24^\circ$ and $\alpha > 28^\circ$ for W1_STShort and W1_STLong, respectively, the IBV breakdown location is close to the locations at symmetric freestream conditions. The decrease in effective leading-edge sweep due to an angle of sideslip of $\beta = -5^\circ$ leads to an only minor change of the breakdown position for the short-strake variant which could not be resolved by the PIV cross sections. The breakdown locations of W1_STLong are positioned more upstream compared to the W1_STShort for the same inflow conditions. They are also located significantly more upstream compared to the long-strake variant at $\beta = 0^\circ$.

The MBV breakdown locations show a similar behavior. In this case, the breakdown position at W1_STShort between $\alpha = 8^\circ$ and $\alpha = 16^\circ$ is only slightly shifted upstream due to the stabilizing effect of the vortex interaction which has already been discussed for the double-delta wing configurations. The breakdown behavior of the MBV also shows the enhanced stabilizing effect of the IBV on the MBV for the long-strake variant, especially, for $\beta = +5^\circ$ and $\beta = 0^\circ$. At $\beta = -5^\circ$, the effect is markedly alleviated, and the breakdown locations are close to each other. At $\alpha = 32^\circ$ and $\beta = +5^\circ$, the breakdown of the long-strake configuration is located more upstream due to the interaction with the fuselage vortex.

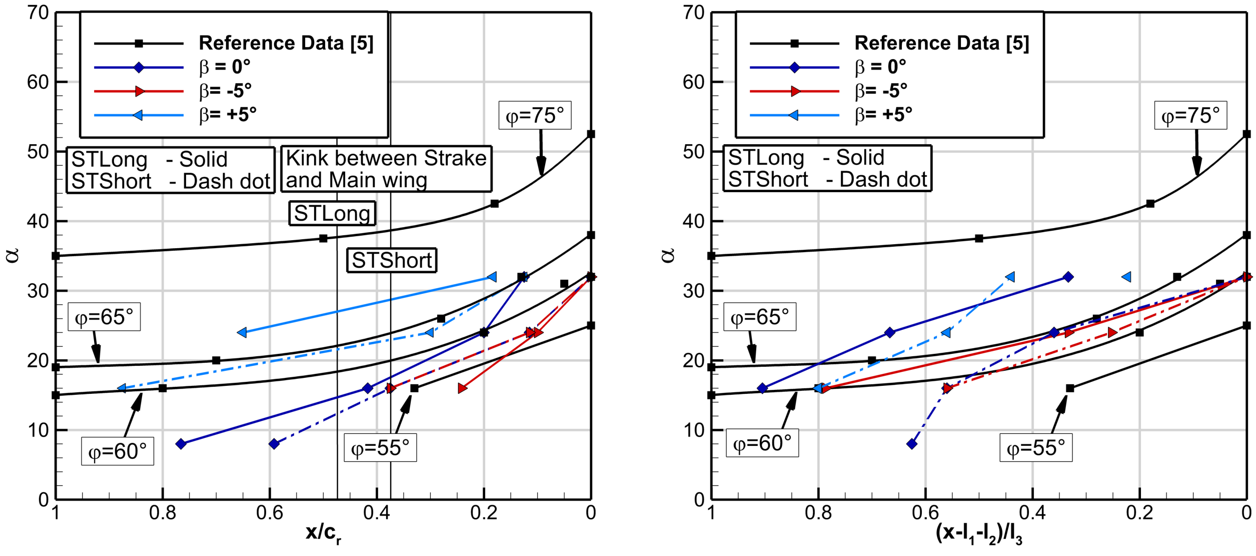

(a) Location of the IBV breakdown

(b) Location of the MBV breakdown

Figure 14 – Vortex-breakdown locations relative to root chord for varying angle of attack for the W1 configurations at $Re = 3.0 \cdot 10^6$. Including reference data taken from [5], [6] and [14].

5.4 Longitudinal and Lateral Stability Characteristics

For the analysis of the longitudinal force and moment coefficients, the location of the pitching moment reference point is discussed. Figure 15 shows the pitching moment coefficient regarding different locations of the moment reference point. The default reference is the reference point of the balance, $x_{ref,bal}$. The red line illustrates the pitching moment coefficient with the surface centroid as the reference point. This is positioned at $x/c_r = 0.551$ and $+0.7\ \%\ l_t$ downstream of $x_{ref,bal}$ for W1_STShort and at $x/c_r = 0.579$ and $+2.3\ \%\ l_t$ downstream of $x_{ref,bal}$ for the long-strake configuration. Furthermore, solid lines depict polars with a downstream shift of the reference point and dash-dot lines represent an upstream shift of the moment reference point. The short-strake configuration exhibits a positive pitching moment for all considered moment reference points except for the $5\ \%\ l_t$ upstream shift of the reference point. This leads to a constant pitching moment close to $C_{my} = 0$ indicating the location converges with the center of pressure. For an angle of attack of $\alpha > 35°$, the pitching moment turns to negative values. The pitching moment of the long-strake variant exhibits a comparable behavior but the most upstream reference point leads to a completely negative pitching moment. The configuration exhibits a less linear behavior compared to W1_STShort and a pitching moment increase is occurring at $\alpha \approx 12°$ resulting from the IBV breakdown at the trailing edge. Comparable to the double-delta wing configurations, the maximum difference of the pitching moments between the maximum shift of the reference point is lower for the short-strake configuration, $\Delta C_{my,xref} = 0.395$, compared to W1_STLong, $\Delta C_{my,xref} = 0.446$. This results from the different vortex characteristics and the swept trailing edge at the short strake configuration. In this region, significant changes can occur due to vortex interaction or breakdown and have a pronounced influence on the pitching moment coefficient caused by the large lever arm.

The lift and pitching moment coefficients and derivatives are shown in Figure 16. The moment reference point is located in the surface centroid. Both configurations exhibit similar trends in the lift as well as the pitching moment coefficient, cf. Figure 16a. This can also be seen in the distribution of the lift derivative, see Figure 16b. The short-strake configuration exhibits a decrease in the lift derivative at a lower angle of attack $\alpha \approx 12°$ and a lower maximum lift coefficient, $C_{L,max} \approx 1.4$ compared to $\alpha \approx 14°$ and $C_{L,max} \approx 1.5$ for the long-strake variant. The trend of the pitching moment is similar for both configurations for $\alpha < 12°$. For higher angles of attack, the long-strake variant exhibits a higher pitching moment derivative resulting in a stronger pitch up tendency.

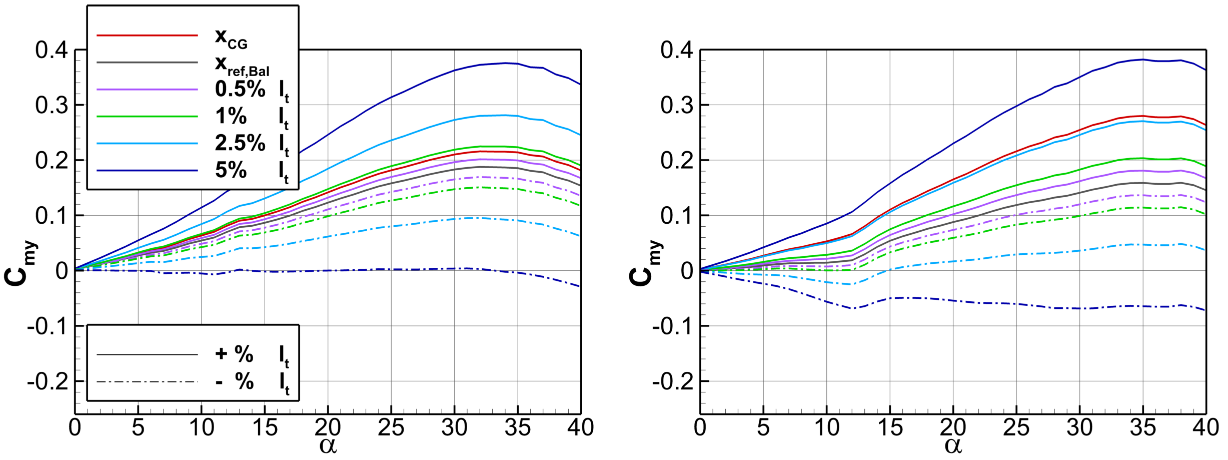

(a) STShort (b) STLong

Figure 15 – Variation of the reference point of the pitching moment.

The forces and moments at an angle of sideslip are discussed by means of Figure 17. The lift and pitching moment coefficients are shown in Figure 17a. The lift coefficient exhibits similar characteristics compared to the symmetric case with a decrease in the lift derivative at lower angles of attack. At higher angles of attack, $\alpha > 28°$, both configurations show a flattening of the lift curve. In contrast to the double-delta wing configuration, no further lift increase occurs at very high angles of attack. The pitching moment is similar for both configurations with a higher pitch-up tendency of the long-strake configuration. In the rolling moment coefficient, see Figure 17b, the windward vortex breakdown is observable by the increase of C_{mx} and the lower angle of divergence $\alpha_{div} \approx 14°$ for W1_STShort compared to $\alpha_{div} \approx 26°$ for W1_STLong. The vortex breakdown at the windward side of the long-strake configuration occurs at $\alpha = 14°$ but the breakdown does not lead to a direct roll reversal and the rolling moment is close to $C_{mx} = 0$ up to an angle of attack of $\alpha \approx 26°$. At this angle of attack, the breakdown at the windward side has reached the apex and the wake-type vortex system is getting unstable. However, at the leeward side, the vortex system is stable, and the leeward vortex induces suction peaks lead to a significant increase in the rolling moment coefficient.

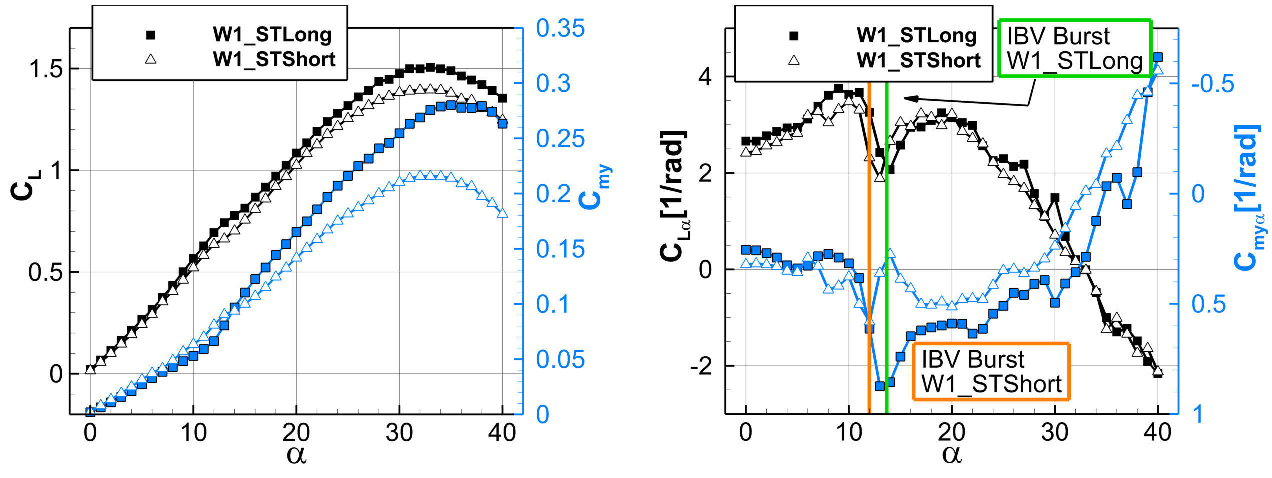

(a) Lift coefficient C_L

(b) Pitching Moment coefficient C_{my}

Figure 16 – Longitudinal aerodynamic coefficients and derivatives for the W1_STShort and W1_STLong configurations versus α at $\beta = 0°$.

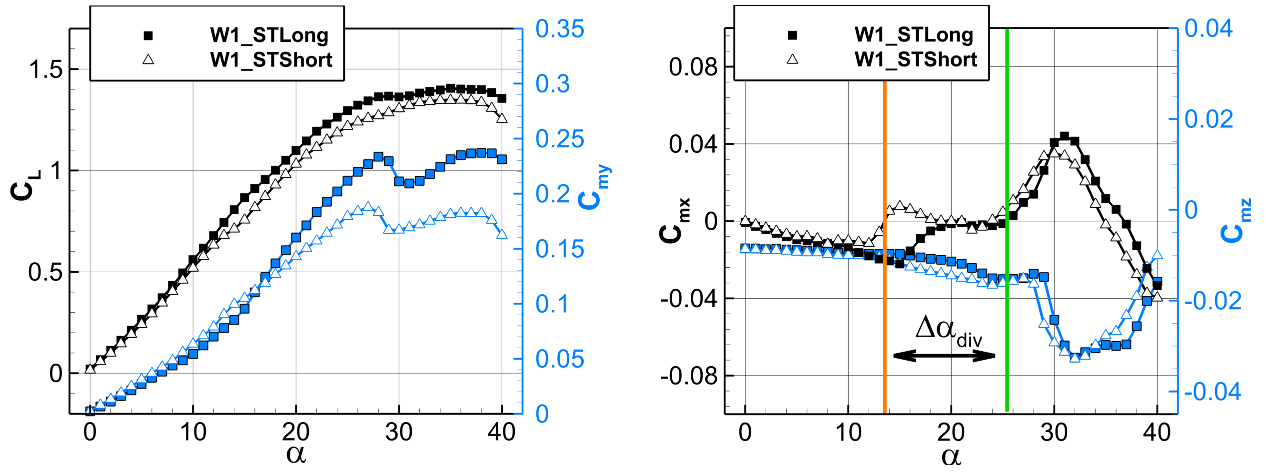

(a) Longitudinal coefficients for lift C_L and pitching moment coefficient C_{my}

(b) Lateral coefficients for rolling C_{mz} and yawing moment C_{mz}

Figure 17 – Longitudinal and lateral aerodynamic coefficients for the W1_STShort and W1_STLong configurations versus α at $\beta = 5°$.

5.5 Influence on Slat Efficiency

The influence and the efficiency of the slat at the different triple-delta wing configurations is discussed in this section. Figure 18a shows the difference in lift coefficient between the configuration with deployed slats (SL22) and the default one. Comparable to the double-delta wing configurations, the slat has a negative influence on the lift for low and medium angles of attack, $\alpha < 24°$, but with less loss of lift. For $\alpha > 24°$, the lift increase does hardly change with the angle of sideslip. Both, short- and long-strake, configurations show a similar lift increase for $\beta = 0°$ and $\beta = 5°$ with a maximum increase of $\Delta C_{L,max} \approx 0.06$ for W1_STShort and $\Delta C_{L,max} \approx 0.095$ for the long-strake configuration at $\beta = 5°$. The maximum lift increase caused by deployed slats for the symmetric case at the long-strake configuration is $\Delta C_{L,max} \approx 0.075$. For angles of attack of $\alpha > 35°$, the lift increase is similar for both configurations and angles of sideslip.

Regarding the lateral stability, the rolling moment coefficient is shown in Figure 18b. The slats have the most impact in the range of $10° < \alpha < 30°$. In this region, the rolling moment increase is delayed and the angle of divergence is shifted to higher angles of attack, $\Delta\alpha_{div,Slat} \approx 14^\circ$ for the short-strake configuration and $\Delta\alpha_{div,Slat} \approx 4^\circ$ for W1_STLong. This indicates a much greater improvement for the short-strake variant but the rolling moment coefficient of the W1_STLong configuration exhibits higher negative values and therefore, is less susceptible and critical to slight changes in flight conditions.

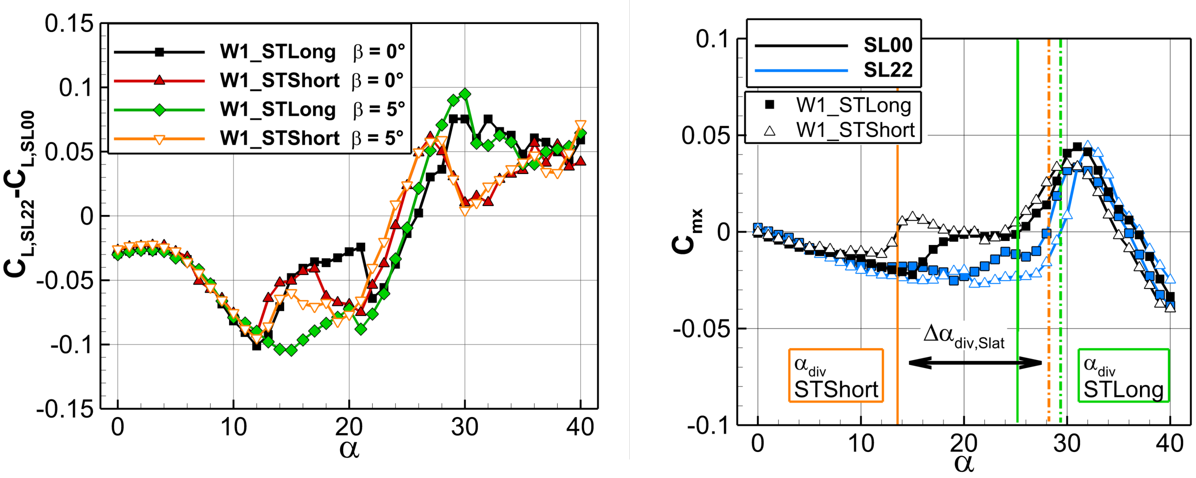

(a) Difference of lift coefficient of slat configuration (SL22) and default configuration (SL00) as function of the angle of attack

(b) Lateral coefficients for rolling C_{mz} and angle of divergence

Figure 18 – Slat efficiency and influence on longitudinal and lateral aerodynamic coefficients for the W1_STShort and W1_STLong configurations versus α.

6. Conclusion

In this study, the influence of the strake length of a double- and a triple-delta wing configuration is discussed by means of force and moment measurements and particle image velocimetry experiments. For the double-delta wing configuration, the shorter strake leads to a more upstream breakdown position or a vortex breakdown at lower angles of attack. The breakdown occurs less abrupt and does not result in a decrease in lift coefficient but the vortex core flow changes directly from jet-type to wake-type core flow. Therefore, for the pitching moment coefficient, the vortex breakdown is not clearly observable. At the long-strake configuration, the pitching moment derivative reaches the highest value caused by the abrupt upstream shift of the inboard vortex (IBV) breakdown location. The reference point of the pitching moment is located more downstream for the long-strake variant and a shift of the reference point has a larger impact on the pitching moment. The analysis of the flow field at the short-strake configuration has shown the significant stabilizing effect of the IBV-midboard vortex (MBV) interaction. The burst IBV at $\alpha = 8^\circ$ is stabilized due to the vortex interaction and is completely stable and merging with the MBV at $\alpha = 16^\circ$. The deployment of leading-edge slats results in a decrease in lift for $\alpha < 20^\circ$ for both, short- and long-strake, configurations and then in an increase up to $\Delta C_L \approx +0.15$ for higher angles of attack at the long-strake configuration. The latter shows a higher efficiency regarding lift increase especially for symmetric freestream conditions. With deployed slats, the angle of divergence is increasing by $\Delta\alpha_{div} \approx 9^\circ$ and $\Delta\alpha_{div} \approx 5^\circ$ for the short- and the long-strake configuration, respectively. Furthermore, the abruptness of the rolling moment reversal of the long-strake variant is decreased.

The triple-delta wing configurations show a comparable behavior regarding the flow field and the vortex breakdown locations. In this case, it is observed that the shorter strake length influences the flow upstream of the main-wing kink. For high angles of attack, the vortex breakdown occurs more upstream for the short-strake configuration even in the front-wing section. The influence of a destabilizing vortex-vortex interaction is observed at $\alpha = 32^\circ$ and $\beta = 5^\circ$ at the long-strake configuration. Here, the fuselage vortex interacts with the MBV directly downstream of the leading-edge kink at $x/c_r = 0.475$ and the MBV breakdown occurs closely downstream. Regarding the short-strake configuration, the fuselage vortex interacts with the MBV due to the shorter strake more downstream relative to the kink.

Both configurations show a similar behavior regarding longitudinal force and moment coefficients and derivatives. With a higher pitch-up tendency for the long-strake configuration. Regarding the lateral coefficients, the rolling moment reversal occurs at higher angles of attack at the long-strake variant. Comparable to the double-delta wing configurations, the leading-edge slat leads to a rolling moment reversal at higher angles of attack for both configurations with a larger shift of the angle of divergence for the short-strake variant and less critical characteristics in the range of $14^\circ < \alpha < 30^\circ$ for both configurations. A lift increase caused by the deployed slats is only occurring for $\alpha > 24^\circ$ and the effect is lower compared to the double-delta wing configuration. But especially for both short-strake variants, the lift increase caused by the slats is present only for considerably larger angles of attack than the marked angle of divergence.

For double- and triple-delta wings, the long-strake configurations exhibit a higher lift coefficient, higher maximum angle of attack and higher maximum lift coefficients. But the abrupt vortex breakdown at the double-delta wing configuration can be lessened and a slightly higher stability regarding the shift of the pitching moment reference point can be reached with the short-strake configurations. Furthermore, both short-strake variants exhibit a more continuous and linear pitching moment behavior.

In future investigations, the leading-edge sweep of the strake and the effect as well as the influence of the slats on the vortex development and interaction will be analyzed taking more geometric variants into account.

Acknowledgements

The project is funded by the Deutsche Forschungsgemeinschaft (DFG, German Research Foundation) – grant number BR1511/13-1. The fruitful cooperation with Airbus Defense and Space is gratefully acknowledged. Furthermore, the authors thank the German Aerospace Center (DLR) for providing the DLR TAU-Code used for the numerical investigations. Moreover, the authors gratefully acknowledge the Gauss Centre for Supercomputing e.V. (www.gausscentre.eu) for funding this project by providing computing time on the GCS Supercomputer SuperMUC at Leibniz Supercomputing Centre (www.lrz.de). The authors also highly appreciate the previous wind tunnel tests by Stefan Pfnür and support by Jan Pfennig.

Copyright Statement

References

[1] S. Hitzel, “Sub- and Transonic Vortex Breakdown Flight Condition Simulations of the F-16XL Aircraft,” *Journal of Aircraft*, vol. 31, no. 4, pp. 868–878, 2016.

[2] C. Breitsamter, “Unsteady flow phenomena associated with leading-edge vortices,” *Progress in Aerospace Sciences*, vol. 44, no. 1, pp. 48 – 65, 2008.

[3] I. Gursul, “Review of Unsteady Vortex Flows over Slender Delta Wings,” *Journal of Aircraft*, vol. 42, pp. 299–319, July 2005.

[4] I. Gursul, R. Gordnier, and M. Visbal, “Unsteady aerodynamics of nonslender delta wings,” *Progress in Aerospace Sciences*, vol. 41, no. 7, pp. 515–557, 2005.

[5] D. L. Kohlman and W. H. Wentz, JR., “Vortex Breakdown on Slender Sharp-Edged Wings,” *Journal of Aircraft*, vol. 8, no. 3, pp. 156–161, 1971.

[6] S. Pfnür and C. Breitsamter, “Leading-Edge Vortex Interactions at a Generic Multiple Swept-Wing Aircraft Configuration,” *Journal of Aircraft*, vol. 56, no. 6, pp. 2093–2107, 2019.

[7] U. Brennenstuhl and D. Hummel, “Vortex Formation over Double-Delta Wings,” *13th Congress of the International Council of the Aeronautical Sciences, International Council of the Aeronautical Sciences Paper 6.6.3, Amsterdam, The Netherlands,*, p. 1133–1146, 1982.

[8] H. W. M. Hoeijmakers, W. Vaatstra, and N. G. Verhaagen, “Vortex Flow over Delta and Double-Delta Wings,” *Journal of Aircraft*, vol. 31, no. 4, pp. 868–878, 1983.

[9] N. Verhaagen, L. Jenkins, S. Kern, and A. Washburn, “A study of the vortex flow over a 76/40-deg double-delta wing,” in *33rd Aerospace Sciences Meeting and Exhibit*, 1995.

[10] X. Zhang, Z. Wang, and I. Gursul, “Interaction of multiple vortices over a double delta wing,” *Aerospace Science and Technology*, vol. 48, pp. 291–307, 2016.

[11] C. J. Obara and J. E. Lamar, “Overview of the cranked-arrow wing aerodynamics project international,” *Journal of Aircraft*, vol. 46, no. 2, p. 355–368, 2009.

[12] J. M. Luckring, M. A. Park, S. M. Hitzel, A. Jirásek, A. J. Lofthouse, S. A. Morton, D. R. McDaniel, A. Rizzi, and M. Tomac, “Synthesis of hybrid computational fluid dynamics results for f-16xl aircraft aerodynamics,” *Journal of Aircraft*, vol. 54, no. 6, pp. 2100–2114, 2017.

[13] J. Zastrow, “Characterizing a multi delta wing for aeroelastic wind tunnnel experiments,” in *IFASD 2019 - International Forum on Aeroelasticity and Structural Dynamics*, 01 2019.

[14] D. Sedlacek and C. Breitsamter, “Aerodynamic characteristics and topology of interfering vortex systems at hybrid delta wings,” in *AIAA SCITECH 2022 Forum*, 2022.

[15] M. Raffel, C. E. Willert, S. T. Wereley, and J. Kompenhans, *Particle Image Velocimetry - A Practical Guide*. Springer Verlag, 2007.

[16] A. Sciacchitano and B. Wieneke, “Piv uncertainty propagation,” *Measurement Science and Technology*, vol. Vol. 27, no. No. 8, 2016.